Magnetotransport across Weyl semimetal grain boundaries

Haoyang Tian,* Vatsal Dwivedi, Adam Yanis Chaou, and Maxim Breitkreiz†
Freie Universität Berlin, Dahlem Center for Complex Quantum Systems and Fachbereich Physik, Arnimallee 14, 14195 Berlin, Germany

(Received 26 September 2025; revised 19 December 2025; accepted 22 December 2025; published 24 February 2026)

A clean interface between two Weyl semimetals features a universal, field-linear tunnel magnetoconductance of $(e^2/h)N_{\mathrm{ho}}$ per magnetic flux quantum, where N_{ho} is the number of chirality-preserving topological interface Fermi arcs. In this work we show that the linearity of the magnetoconductance is robust with respect to interface disorder. The slope of the magnetoconductance changes at a characteristic field strength B_{arc}—the field strength for which the time taken to traverse the Fermi arc due to the Lorentz force is equal to the mean inter-arc scattering time. For fields much larger than B_{arc}, the magnetoconductance is unaffected by disorder. For fields much smaller than B_{arc}, the slope is no longer determined by N_{ho} but by the simple fraction $N_{\mathrm{L}}N_{\mathrm{R}}/(N_{\mathrm{L}}+N_{\mathrm{R}})$, where N_{L} and N_{R} are the numbers of Weyl-node pairs in the left and right Weyl semimetal, respectively. We also consider the effect of spatially correlated disorder potentials, where we find that B_{arc} decreases exponentially with increasing correlation length. Our results provide a possible explanation for the recently observed robustness of the negative linear magnetoresistance in grained Weyl semimetals.

DOI: 10.1103/99q1-37q7

I. INTRODUCTION

Weyl semimetals (WSMs) have emerged as a paradigmatic platform for exploring gapless topological phases of matter. Characterized by topologically protected band crossings, termed Weyl nodes [1,2], the low-energy physics is governed by the Weyl Hamiltonian $H=\chi\,\boldsymbol{p}\cdot\boldsymbol{\sigma}$, where $\chi=\pm 1$ denotes the chirality, $\boldsymbol{p}$ the momentum, and $\boldsymbol{\sigma}$ the vector of Pauli matrices corresponding to (pseudo) spin. Weyl nodes always occur in pairs of opposite chirality and can only be gapped out by pairwise annihilation.

WSMs exhibit a range of anomalous transport phenomena rooted in their chiral electronic structure. Among the most striking features are the negative longitudinal magnetoresistance induced by the chiral anomaly. In the presence of an applied magnetic field, the chiral anomaly [3,4] of Weyl nodes manifests in the lowest Landau level: The Landau quantization of the Weyl node leads to a chiral zeroth Landau level moving parallel or antiparallel to the magnetic field depending on the chirality. The resulting chiral magnetic effect is theoretically expected to manifest as a positive longitudinal magnetoconductance [5–8]. Experimentally identifying the chiral magnetic effect remains challenging due to extrinsic effects, such as current jetting, the fact that Weyl nodes do not typically reside at the Fermi level, and are not the sole charge carriers in the system [9–11].

While most such experiments are performed on single crystals, Ref. [12] reports the observation of a particularly robust chiral magnetic effect in a grained WSM with randomly oriented crystallites. On the theoretical side, some of us have recently shown that the chiral magnetic effect can occur at interfaces between different or differently oriented WSMs [13,14] in the form of a universal tunnel magnetoconductance that does not depend on the Fermi momentum and velocity of the Weyl fermions,

$$G_0(B)=\frac{e^3}{h^2}|\boldsymbol{A}\cdot\boldsymbol{B}|, \tag{1}$$

where $|\boldsymbol{A}\cdot\boldsymbol{B}|$ is the magnetic flux through the interface area $\boldsymbol{A}$. While the original chiral magnetic effect is rooted only in the bulk Weyl fermions, the tunnel magnetoconductance across an interface involves topological interface states. These are related to the well-established WSM surface states, called Fermi arcs, which are open contours of chiral modes connecting the projections of *opposite-chirality* bulk Weyl nodes on the surface Brillouin zone [1]. Fermi arcs also exist at interfaces between WSMs, where they can connect Weyl nodes of the *same chirality* on opposite sides of the interface [13,15–21], as illustrated in Fig. 1. In the presence of a magnetic field perpendicular to the interface, such chirality-preserving (homochiral) interface Fermi arcs transmit the chiral Landau level of bulk Weyl fermions, while filtering out other modes, leading to the universal tunnel magnetoconductance $G(B)=N_{\mathrm{ho}}G_0(B)$, where N_{ho} is the number of pairs of homochiral Fermi arc. This mechanism can always be extended to a setting consisting of a series of interfaces [22], thus leading to a chiral magnetic effect of a grained WSM.

In this work we investigate how robust this Fermi-arc-mediated magnetotransport across interfaces is to interface disorder. While it is known that surface Fermi arcs contribute to in-plane transport in a disorder-robust fashion [23–33], the robustness of the Fermi-arc mediated magnetotransport across a WSM interface is not obvious. To address this question, we develop a hybrid approach consisting of both

*Contact author: haoyang.tian@uni-koeln.de
†Contact author: breitkr@physik.fu-berlin.de

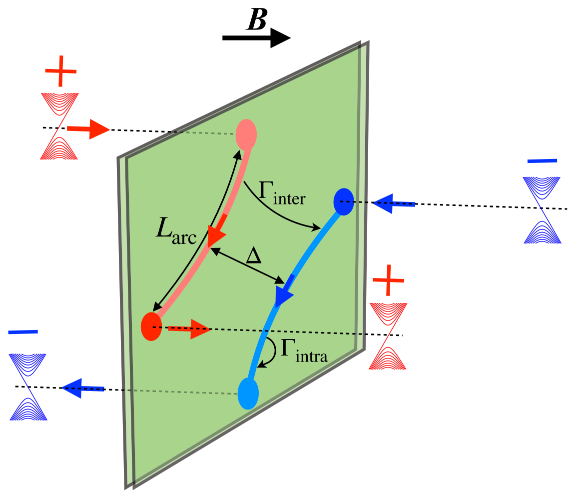

FIG. 1. WSM interface in momentum space (green area) with two interface Fermi arcs (red/blue lines) connecting the projections of Weyl nodes (red/blue circles for positive/negative chirality). Intra- and inter-arc scattering is depicted, as well as the particle flow (red/blue arrows) in the presence of a magnetic field $\boldsymbol{B}$ normal to the interface.

Landauer-Bütticker and semiclassical Boltzmann transport formalisms. The former accounts for the chiral anomaly, while the latter incorporates the effects of disorder. We corroborate our analytical predictions by way of lattice simulations on a tight-binding model. Our main result is that the linearity of the magnetoconductance is robust and features two different slopes in the limits of fields being much larger and much smaller than $B_{\rm arc}$—a characteristic field strength at which the time it takes to traverse a Fermi arc driven by the Lorentz force is equal to the mean time between inter-arc scattering events. For fields much larger than $B_{\rm arc}$, the magnetoconductance is identical to the clean-interface case. For fields much smaller than $B_{\rm arc}$, the magnetoconductance becomes a simple fraction of $G_0(B)$. The resulting linear, slope-changing positive magnetoconductance qualitatively agrees well with the experimental measurement of the magnetoconductance in a grained Weyl semimetal [12].

This paper is organized as follows. In Sec. II we introduce the Landauer-Boltzmann approach to the tunnel magnetoconductance behavior of disordered interfaces and discuss the generic properties of the conductance. In Sec. III we test and exemplify the transport behavior on a minimal lattice model introduced in Sec. III A. Specifically, in Sec. III B we deploy our hybrid approach on the lattice model and compare with full-quantum transport simulations. In Sec. III C we explore the special case of weakly coupled interfaces with magnetic breakdown. In Sec. III D we discuss the disorder-activated contribution of nonchiral Landau levels. We conclude in Sec. IV.

II. ANALYTICAL MODEL

We start by considering a minimal model of an interface between two WSMs, each featuring a single pair of opposite-chirality Weyl nodes whose position changes across the interface, as sketched in Fig. 1. Let both Fermi arcs be of length $L_{\rm arc}$ and consider an applied magnetic field B perpendicular to the interface. In the bulk, the magnetic field gives rise to Landau levels at the Weyl nodes with a chiral lowest Landau level that moves parallel/antiparallel to the field depending on the Weyl-node chirality. Bulk currents from the chiral Landau levels on either side of the interface reconnect via interface currents carried along Fermi arcs. While the formation of chiral Landau levels is a purely quantum-mechanical effect, electron flow along the Fermi arcs can be understood semiclassically as a result of the Lorentz force changing the momentum by $|d\boldsymbol{k}|/dt = v/l_B^2$, where $l_B = \sqrt{\hbar/eB} \approx 26$ nm $\sqrt{1/B[\mathrm{T}]}$ is the magnetic length and v is the Fermi-arc velocity. According to this equation of motion, the dwell time of a particle on a Fermi arc is

$$\tau_{\rm dwell} = \frac{L_{\rm arc} l_B^2}{v} = \frac{\hbar L_{\rm arc}}{evB}. \tag{2}$$

For a clean interface, the conductance is simply that of the chiral (bulk) Landau level $G_0(B)$, which is perfectly transmitted via the Fermi arc, while contributions from higher Landau levels perfectly reflect [13]. In the presence of disorder, both effects are modified. The correction due to disorder-activated contribution of nonchiral Landau levels, however, stays negligible in most cases, as will be shown separately in Sec. III D. To get a sense of the effect of disorder on the transmission via the Fermi arcs, note that for well-separated Weyl nodes, $L_{\rm arc} \sim 0.1$ Å^{-1}, even at relatively large fields of $B \sim 1$ T, the dwell time is on the order of $\tau_{\rm dwell} \sim 1$ μm$/v$. Disorder introduces a finite lifetime $\tau_{\rm life}$, which, depending on the purity of the interface, may well be shorter than $\tau_{\rm dwell}$. For this likely case of $\tau_{\rm life} \lesssim \tau_{\rm dwell}$ one would expect particles to scatter within Fermi arcs (intra-arc scattering), as well as between the arcs (inter-arc scattering), the latter type of scattering event being between counterpropagating channels.

A. Landauer-Boltzmann transport approach

To calculate the conductance across the interface in the presence of disorder, we consider the in- and outgoing chiral Landau levels in the bulk of the two WSMs, whose degeneracy is $N_B = (e/h)AB$, where AB is the magnetic flux through the interface. To linear order in the applied voltage, the nonequilibrium occupation of states f can be expressed in terms of the deviation μ of the chemical potential from the Fermi level as $f = n_F + n_F' \mu$, where n_F is the equilibrium occupation and n_F' its derivative with respect to energy. We denote these chemical-potential deviations as $\mu_\pm(\kappa)$, where $\pm$ corresponds to the right/left-moving chiral states with chirality $\chi = \pm$ and $\kappa = \pm 1$ corresponds to the right/left WSM. According to the Landauer-Büttiker transport approach, the conductance is given by

$$G(B) = G_0(B)\, T(B), \tag{3}$$

where $G_0(B)$ is the conductance at full transmission of the chiral Landau levels and $T(B)$ is the transmission probability. Expressing the conductance in terms of the occupation functions $f = n_F + n_F' \mu$, the transmission probability can be expressed in terms of $\mu_\pm(\kappa)$ as

$$T(B) = \frac{\sum_\chi \chi \mu_\chi(\pm 1)}{\mu_+(-1) - \mu_-(1)}, \tag{4}$$

which is the occupation difference of countermoving modes (same in the right and left WSMs due to particle conservation) divided by the difference between left and right WSMs, $\mu_+(-1) - \mu_-(1)$, which corresponds to the applied voltage.

To calculate the nonequilibrium potentials $\mu_\pm(\kappa)$ in the presence of disorder we consider the Boltzmann transport equation (BE), which describes the dynamics of a nonequilibrium occupation function f of the Fermi arcs as

$$\frac{\mathrm{d}f}{\mathrm{d}t} = \frac{d\boldsymbol{k}}{dt} \cdot \partial_{\boldsymbol{k}} f = \left(\frac{\partial f}{\partial t}\right)_{\text{coll}}, \tag{5}$$

where $d\boldsymbol{k}/dt$ is given by the Lorentz force and the right-hand side is the collision integral that perturbatively incorporates scattering processes. We used that f is spatially homogeneous and $\partial f/\partial t = 0$ in the steady state. We use $f = n_F + n_F'\mu$ and parametrize μ on the Fermi arc by allowing the parameter κ in $\mu(\kappa)$ to assume values in the range $\kappa \in [-1, 1]$, where $\kappa = \pm 1$ corresponds to the ends of the arc that merge with the bulk of the right/left WSM. Assuming zero temperature, approximating the collision integral to lowest order in the perturbation [34], and using the Fermi-arc parametrization and Lorentz-force expression introduced above, the BE reads

$$\chi\,\partial_\kappa \mu_\chi(\kappa) = \sum_{\chi'=\pm} \int_{-1}^{1} d\kappa' \beta^{-1}_{\chi\kappa,\chi'\kappa'} [\mu_{\chi'}(\kappa') - \mu_\chi(\kappa)], \tag{6}$$

where

$$\beta^{-1}_{\chi\kappa,\chi'\kappa'} = \beta^{-1}_{\chi'\kappa',\chi\kappa} = \frac{L_{\text{arc}}^2 l_B^2}{v_\kappa v_{\kappa'}} \Gamma_{\chi'\kappa',\chi\kappa} \tag{7}$$

is the dwell-time weighted scattering rate $\Gamma_{\chi'\kappa',\chi\kappa}$ (up to a constant) between the state at $(\chi\kappa)$ and $(\chi'\kappa')$, such that $\sum_{\chi'} \int d\kappa' \beta^{-1}_{\chi\kappa,\chi'\kappa'} = \tau_{\text{dwell}}/\tau_{\text{life}}$.

B. Approximate analytical solution

Before we solve the BE in the low-field limit and (numerically) in an explicit microscopic model, we here consider an analytically tractable simplified model to better elucidate the magnetoconductance mechanism. We take the intra- and inter-arc scattering rates to assume two constant values, $\Gamma_{\chi\kappa,\chi'\kappa'} = \Gamma_{\text{intra}}$ for $\chi = \chi'$ and $\Gamma_{\chi\kappa,\chi'\kappa'} = \Gamma_{\text{inter}}$ for $\chi = -\chi'$ (this simplification is only used in this subsection). Solving for $\mu_\chi(\kappa)$ under the boundary condition of a given voltage across the interface, we obtain

$$\mu_\chi(\kappa) = \frac{\chi}{2} \frac{e^{(1-\chi\kappa)/2\beta}(\gamma - 1) + \gamma\beta(1 - e^{1/\beta})}{e^{1/\beta}(\gamma - 1) + \gamma\beta(1 - e^{1/\beta})} \tag{8}$$

leading to the transmission probability

$$T(B) = 1 - \frac{1}{2}\left(\frac{\beta\gamma}{1-\gamma} + \frac{1}{1 - e^{-1/\beta}}\right)^{-1}, \tag{9}$$

where

$$\gamma \equiv \frac{\Gamma_{\text{intra}} - \Gamma_{\text{inter}}}{\Gamma_{\text{intra}} + \Gamma_{\text{inter}}}, \tag{10}$$

$$\beta \equiv \frac{\tau_{\text{dwell}}}{\tau_{\text{life}}} = \frac{l_{\text{mfp}}}{L_{\text{arc}} l_B^2} = \frac{e|B|}{\hbar} \frac{l_{\text{mfp}}}{L_{\text{arc}}}. \tag{11}$$

The parameter $\beta \sim 0.15\,|B[\text{T}]|\, l_{\text{mfp}}[\mu\text{m}] L_{\text{arc}}^{-1}[\text{Å}]$ is the flux through the area spanned by the mean free path $l_{\text{mfp}} = \tau_{\text{life}} v$ and L_{arc}^{-1} in units of the flux quantum h/e. For well-separated Weyl nodes, β will be small in the experimentally relevant parameter regimes. The parameter $\gamma \in [-1, 1]$ characterizes the dominant type of scattering. Spatially smooth (or correlated) disorder will tend to increase intra-arc scattering and lead to $\gamma \to 1$, while pointlike (or uncorrelated) disorder would lead to similar scattering rates and thus $\gamma \to 0$. The regime $-1 \leqslant \gamma \leqslant 0$ corresponds to dominant inter-arc scattering, which, though less realistic, is included for completeness.

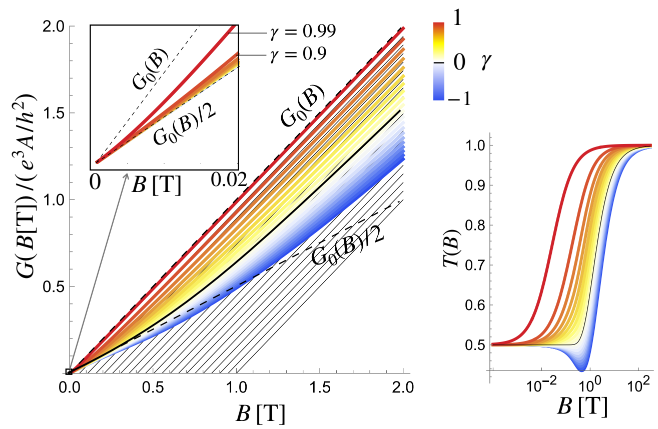

FIG. 2. Left: Conductance as a function of the magnetic field for $\gamma = 0$ (black solid line) and all other γ (colored lines). Dashed lines indicate the asymptotic conductance at low fields, $G_0(B)/2$, and large fields, $G_0(B)$ (thin gray lines for different γ). Upper inset shows a close-up at small fields. Right: Transmission probability $T(B) = G(B)/G_0(B)$. The parameters are $L_{\text{arc}} = 0.2$ Å^{-1}, $l_{\text{mfp}} = 1$ μm.

The transmission probability is a nonanalytic function of the field, whose behavior is shown in Fig. 2. For $0 \leqslant \gamma \leqslant 1$ it increases monotonically from 0.5 to 1, while for (the less relevant regime) $-1 \leqslant \gamma \leqslant 0$ it first slightly decreases to reach a minimum at $\beta \lesssim 0.3$ and $T(B) \gtrsim 0.4$. The limiting behavior near $T(0)$ and $T(\infty)$ is, however, γ independent.

For small fields, the transmission saturates at $T(0) = \frac{1}{2}$; the asymptotic behavior at large fields is $T(B)|_{\beta\to\infty} = 1 - \beta_0/\beta$, where $\beta_0 = (1-\gamma)/2$. This yields low- and high-field magnetoconductances of

$$G(B) = \begin{cases} G_0(B)/2 & \text{for } B \ll B_{\text{arc}} \\ G_0(B) - G_0(B_{\text{arc}}) & \text{for } B \gg B_{\text{arc}}, \end{cases} \tag{12}$$

where the characteristic field B_{arc} corresponding to β_0 reads

$$B_{\text{arc}} = \frac{\hbar}{e}\frac{1-\gamma}{2l_{\text{mfp}}} L_{\text{arc}} \equiv \frac{\hbar}{e}\frac{L_{\text{arc}}}{l_{\text{arc}}} \approx \frac{3(1-\gamma)}{l_{\text{mfp}}[\mu\text{m}] L_{\text{arc}}^{-1}[\text{Å}]}\ \text{T}, \tag{13}$$

where $l_{\text{arc}} \equiv 2l_{\text{mfp}}/(1-\gamma) = v/(\Gamma_{\text{inter}} L_{\text{arc}})$ is the mean free path between inter-arc scattering events and thus the characteristic length for which a particle does not change the arc. Note that $\tau_{\text{arc}} \equiv l_{\text{arc}}/v$ can be interpreted as a Fermi-arc lifetime and B_{arc} as the characteristic field at which the arc dwell time is equal to the arc lifetime, $\tau_{\text{dwell}} = \tau_{\text{arc}}$; it is independent of Γ_{intra}.

C. Universal low-field limit

An analytically tractable limit of the full BE is the low-field regime, $\tau_{\mathrm{dwell}} \gg \tau_{\mathrm{life}}$, which we discuss in the following without limiting ourselves to the simplified model. We consider N_L positive-chirality modes in the left WSM that move to the right, all at the occupation μ_+, and N_R negative-chirality modes in the right WSM that move to the left, all at the occupation μ_-. The conductance generalized to this case is given by

$$G(B) = \frac{\sum_a \chi_a \mu_a(\pm 1)}{\mu_+ - \mu_-} G_0(B), \tag{14}$$

where the sum runs over all chiral modes, and the BE generalizes to

$$\chi_a \partial_\kappa \mu_a(\kappa) = \sum_{a'} \int d\kappa' \beta^{-1}_{a\kappa,a'\kappa'}[\mu_{a'}(\kappa') - \mu_a(\kappa)]. \tag{15}$$

In the limit of dwell time being much larger than the lifetime, $\beta_{a\kappa,a'\kappa'} \to 0$, the solution assumes the form

$$\mu_a(\kappa) = e^{-(1+\chi_a\kappa)/\kappa_a}\mu_{\chi_a} + \epsilon_a(\kappa), \tag{16}$$

where $\epsilon_a(\kappa) \sim \kappa_a \sim \beta \to 0$, which can be proven straightforwardly by inserting it into the BE. Hence, in this limit, the occupations fall to the equilibrium values (zero) quickly when propagating along the arc, so that $\mu_a(1) = 0$ for $\chi_a = +$ and $\mu_a(-1) = 0$ for $\chi_a = -$. Equating the conductance calculated in the left and right leads in Eq. (14), one obtains $N_{\mathrm{L}}\mu_+ + N_{\mathrm{R}}\mu_- = 0$. Inserting it back into (14) gives the result

$$G(B) = \frac{N_{\mathrm{L}} N_{\mathrm{R}}}{N_{\mathrm{L}} + N_{\mathrm{R}}} G_0(B). \tag{17}$$

In the low-field limit, the conductance thus assumes a universal fraction of $G_0(B)$, given by the numbers of Weyl nodes in the two WSMs.

D. Summary and interpretation of the analytical results

We first note that since only inter-arc scattering leads to current relaxation, transmission through the interface is unaffected by disorder if the Fermi-arc lifetime—the time between *inter-arc* scattering events—is much longer than the dwell time, $\tau_{\mathrm{arc}} \gg \tau_{\mathrm{dwell}} \propto 1/B$.

In the limit of large magnetic fields we thus obtain for a minimal model of a single pair of homochiral Fermi arcs $G(B) = G_0(B) - G_0(B_{\mathrm{arc}})$, where the slope $dG(B)/dB$ is identical to the universal clean-interface case. Interpolation of the linear magnetoconductance at high fields towards zero field, can give a characteristic offset $G(0) = -G_0(B_{\mathrm{arc}})$ that depends on the Fermi-arc length and lifetime. For an arbitrary interface the clean-interface conductance is given by $N_{\mathrm{ho}}G_0(B)$, where N_{ho} is the number of homochiral Fermi-arc pairs.

In the weak-field limit, i.e., $\tau_{\mathrm{arc}} \ll \tau_{\mathrm{dwell}}$, scattering between Fermi arcs leads to an equalized probability of exiting the interface via any of the $N_{\mathrm{L}} + N_{\mathrm{R}}$ chiral bulk modes in the left and right WSMs, leading to a universal low-field magnetoconductance $G(B)/G_0(B) = N_{\mathrm{L}}N_{\mathrm{R}}/(N_{\mathrm{L}} + N_{\mathrm{R}})$ (which is 1/2 in the minimal model of two Weyl nodes). This is a momentum-space analog of the fractionally quantized conductance across a graphene *p-n* junction in the quantum Hall regime, where the equilibration of copropagating edge states along the junction in *real* space similarly leads to scattering into all outgoing modes with equal probability and hence, a fractionally quantized conductance [35,36].

In the intermediate regime of $\tau_{\mathrm{arc}} \sim \tau_{\mathrm{dwell}}$, the transmission probability changes in a model detail dependent way. In the minimal model of a single pair of Weyl nodes, when inter-arc (intra-arc) scattering dominates, it becomes more likely for a particle to exit on the opposite (same) Fermi arc, thereby giving a conductance slightly smaller (larger) than $G_0(B)/2$.

III. NUMERICAL SIMULATIONS

We now substantiate the discussion of the previous section by numerical computations on an explicit lattice model [37].

A. Lattice model

We consider two WSMs labeled by $A \in \{\mathrm{L}, \mathrm{R}\}$, described by the Bloch Hamiltonians

$$\mathcal{H}_A(k_x, \boldsymbol{k}) = \sin k_x \tau^x + \eta_y^A(\boldsymbol{k})\tau^y + (1 + 2\cos k_0 - \cos k_x - \cos k_y - \cos k_z)\tau^z, \tag{18}$$

where Pauli matrices τ^a represent a pseudospin degree of freedom, $\boldsymbol{k} = (k_y, k_z)$, and the lattice constant is set to unity (but is reinserted where necessary). The parameter k_0 determines the positions of the Weyl nodes, which lie in the $k_x = 0$ plane at $\boldsymbol{k}_{\mathrm{L}} = \pm(k_0, k_0)$ for $A = \mathrm{L}$ and $\boldsymbol{k}_{\mathrm{R}} = \pm(k_0, -k_0)$ for $A = \mathrm{R}$. Accordingly,

$$\eta_y^{\mathrm{L}}(\boldsymbol{k}) = \sin k_0(\sin k_y - \sin k_z)/\sin|\boldsymbol{k}_{\mathrm{L}}|, \tag{19}$$

$$\eta_y^{\mathrm{R}}(\boldsymbol{k}) = \sin k_0(\sin k_y + \sin k_z)/\sin|\boldsymbol{k}_{\mathrm{R}}|. \tag{20}$$

An interface at $x = 0$ between the WSMs $A = \mathrm{L}$ to the left and $A = \mathrm{R}$ to the right is introduced by transformation into real space in the x direction and reducing the hopping across the interface by the factor $t \in [0, 1]$. For decoupled WSMs ($t = 0$) Fermi arcs given by $\eta_y^A(\boldsymbol{k}) = 0$ are straight perpendicular lines joining the nodes of the corresponding WSM and crossing each other near $\boldsymbol{k} = \boldsymbol{0}$ (at low energy). Turning on the interface coupling t, the Fermi arcs hybridize and the crossing becomes an anticrossing with a minimum separation Δ between the arcs, as illustrated in Fig. 1.

We model disorder by a random on-site potential on the interface, $V(\boldsymbol{r})$, with

$$\langle V(\boldsymbol{r})\rangle = 0, \quad \langle V(\boldsymbol{r})V(\boldsymbol{r}')\rangle = W^2 f(\boldsymbol{r} - \boldsymbol{r}'), \tag{21}$$

where $\boldsymbol{r} = (y, z)$ is the position on the interface, $\langle \cdots \rangle$ denotes average over disorder configurations, W parametrizes the magnitude of the disorder potential, and $f(\boldsymbol{r} - \boldsymbol{r}')$ encodes the disorder autocorrelation. We choose

$$f(\boldsymbol{r}) = \frac{1}{\pi\xi^2} e^{-|\boldsymbol{r}|^2/\xi^2}, \tag{22}$$

where ξ is the disorder correlation length. Uncorrelated disorder is obtained in the limit $\xi \to 0$.

We numerically compute the conductance across such an interface using the KWANT PYTHON package [38]. We consider a system with a cross section of 40×40 unit cells in

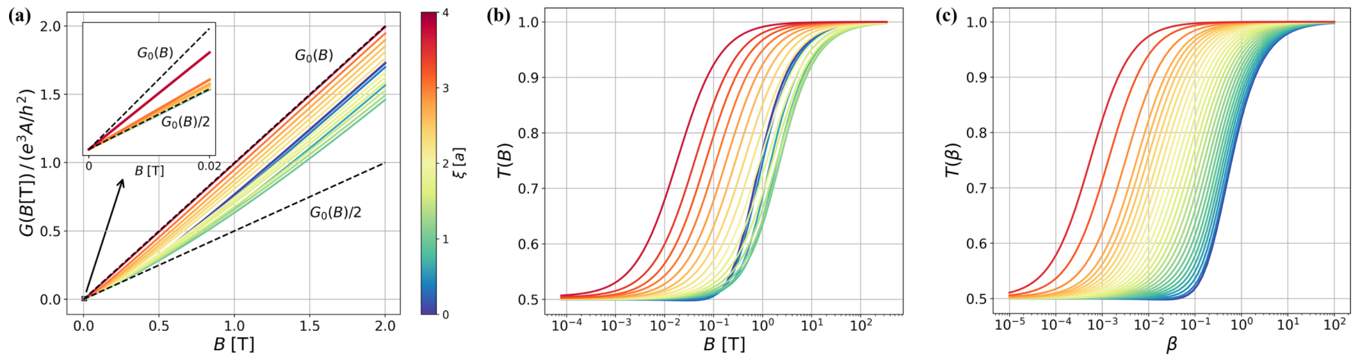

FIG. 3. (a) Conductance $G(B)$ for the WSM model, Eq. (18), with random correlated disorder, Eq. (21), based on the hybrid Landauer-Boltzmann approach for different disorder correlation lengths ξ (cf. Fig. 2). (b) Transmission $T(B) = G(B)/G_0(B)$ as a function of B and (c) as a function of β. Model parameters are $t = 0.4$ ($\Delta \approx 1/a$), $L_{\rm arc} = 0.2/a$, $l_{\rm mfp} = 10^4 a$, $a = 1$ Å.

the y and z directions, with periodic boundary conditions. The scattering region consists of the two interface layers of the right/left WSM as given by Eq. (18) but with the interface hopping suppressed by the factor t. Each interface layer is attached to the right/left lead, consisting of the right/left WSM from Eq. (18). On-site Anderson disorder is added to each site in the scattering region, sampled from a distribution that is taken to be either a Gaussian of width W and correlation length ξ or, for uncorrelated disorder, a uniform distribution on $(-W\sqrt{3}, W\sqrt{3})$ (such that the variance is W^2). The conductance is averaged over 300 disorder realizations. The results of the numerical simulations will be discussed below, in comparison with those of the Landauer-Boltzmann approach.

B. Landauer-Boltzmann approach

For the correlated-disorder model, the scattering rate in the BE (6) is given by [34]

$$\Gamma_{\boldsymbol{k},\boldsymbol{k}'} = W^2 f(\boldsymbol{k}-\boldsymbol{k}')|\langle\Psi_{\boldsymbol{k}}|\Psi_{\boldsymbol{k}'}\rangle|^2, \tag{23}$$

where $f(\boldsymbol{k}) = e^{-k^2\xi^2/4}/\xi\pi\sqrt{2}$ is the Fourier-transformed correlation function $f(\boldsymbol{r})$ and $|\Psi_{\boldsymbol{k}}\rangle$ are Fermi-arc states.

For correlated disorder ($\xi > 0$), the typical momentum change upon scattering is limited by the inverse correlation length $|\boldsymbol{k}-\boldsymbol{k}'| \lesssim 1/\xi$. Inter-arc scattering is therefore strongly suppressed if $1/\xi$ is smaller than the Fermi-arc separation Δ. Otherwise, for $1/\xi \gtrsim \Delta$, both inter- and intra-arc scattering should be present. Thus, comparing with the analytic solution in Fig. 2, we expect $\xi \gtrsim 1/\Delta$ to correspond to the limit $\gamma \to 1$ and $\xi \lesssim 1/\Delta$ to the limit $\gamma \to 0$. As mentioned above, we do not expect to find dominant inter-arc scattering (i.e., $-1 < \gamma < 0$) for any ξ and thus we expect the transmission to lie between 0.5 and 1.

To calculate the conductance, we solve the BE (6) for the microscopic model, Eq. (18). The dwell time $\tau_{\rm dwell}^{-1} = v/L_{\rm arc}l_B^2$ in the BE is momentum dependent due to the (weak) momentum dependence of the velocity v. The calculation of the velocity and the spinor overlap $\langle\Psi_{\boldsymbol{k}}|\Psi_{\boldsymbol{k}'}\rangle$ is detailed in the Appendix. The BE is solved numerically via a discretization of the arcs in momentum space.

The resulting conductance $G(B)$ and transmission $T(B) = G(B)/G_0(B)$ are plotted in Fig. 3 for different correlation lengths ξ. The parameters in Fig. 3 give a characteristic crossover field of $B_{\rm arc} \approx (1-\gamma)$ T and a Fermi-arc separation $\Delta \approx 1/a = 1$ Å^{-1}. The plots confirm the behavior anticipated from the analytic solution: The transmission lies within the expected range of $0.5 < T(B) < 1$, whereby $T(B) = 1$ for $B \gg B_{\rm arc}$ and $T(B) = 1/2$ for $B \gg B_{\rm arc}$. Regarding the dependence on ξ, we find that $B_{\rm arc}$ goes to zero for $\xi \gg 1/\Delta$, as expected from the exponentially suppressed inter-arc scattering ($\gamma \to 1$).

Note that due to the additional dependence of the scattering rate (23) on the wave-function overlap, the ratio of life and dwell times (parameter β in the simplified model) depends weakly on ξ. As a result, in the crossover regime $\xi \sim 1/\Delta$, the ξ dependence of the transmission at a fixed field shows a nonmonotonic behavior, visible more clearly in Fig. 4 discussed below. To make a better comparison with the analytic solution, we determine the life and dwell times for the lattice model and plot the transmission as a function of β, shown in Fig. 3(c). The plot clearly shows that, indeed, for a fixed β, the transmission increases monotonically with ξ, as expected (cf. Fig. 2 right).

Finally, in Fig. 4, we plot the transmission $T(B) = G(B)/G_0(B)$ [where $G_0(B)$ is the theoretical clean-interface conductance (1)] as a function of the scattering correlation length ξ for the full quantum simulation as well as the Landauer-Boltzmann approach. The two results are in agreement (without any fitting parameter) even for a relatively large disorder strength $W = 0.2$, and the agreement improves further with decreasing W [Fig. 4(b)]. The largest deviation at small fields is attributed to small corrections arising from disorder-activated contributions of nonchiral Landau levels, discussed further below.

C. Magnetic breakdown at weakly coupled interfaces

In the above analysis, we assumed semiclassical transport along the interface Fermi arcs, which is justified if the arcs are always separated by a distance larger than $l_B^{-1} \approx 0.004$ Å$^{-1}\sqrt{B[\rm T]}$. Since this distance is very small at realistic magnetic fields, the above results apply to most realistic interfaces.

At an interface with a particularly weak tunnel coupling, which may be purposefully designed by encapsulating an

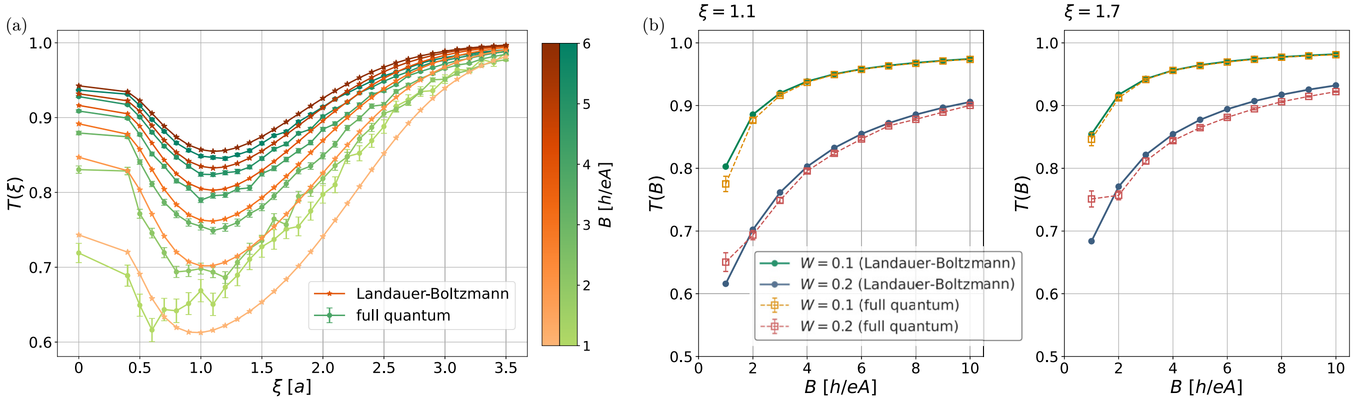

FIG. 4. (a) Transmission $T(B) = G(B)/G_0(B)$ as a function of the scattering correlation length ξ for different magnetic field strength ($B[h/eA]$ is the number of flux quanta through the interface area A). The plot shows results from the Landauer-Boltzmann approach and the full-quantum simulation of a 40×40 interface. Model parameters are $t = 0.4$, $W = 0.2$, and energy $E = 0.1$. (b) Transmission as a function of B for two different ξ and W values. Other parameters as in (a) [37].

insulating layer between the WSMs, the semiclassics break down. Here, the minimal separation at the avoided crossing of the decoupled Fermi arcs is set by the weak coupling across the interface and can become sufficiently small. In this case, particles can quantum tunnel between the arcs—a phenomenon called magnetic breakdown [13,39]. As a result, the transmission probability is suppressed, which in the clean case has been quantified as [13]

$$T_{\rm MB}(B) = 1 - e^{-B_0/B}, \quad B_0 = \frac{\pi}{4}\Delta^2 \tan\theta, \tag{24}$$

where B_0 is the breakdown field that depends only on the minimum separation Δ (see Fig. 1) and the opening angle 2θ of the arcs. The suppressed transmission leads to a saturation of the conductance, $G(B \to \infty) \to G(B_0)$.

The analytical Landauer-Boltzmann approach does not capture the effect of magnetic breakdown since the motion along the arcs is treated semiclassically. The numerical simulation for a weakly coupled, disordered interface is shown in Fig. 5. The comparison with the clean case shows that the disorder only weakly modifies the qualitative behavior dictated by magnetic breakdown, with disorder effects being negligible in the large field regime ($B \gg B_0$).

D. Contributions from nonchiral Landau levels

The universality of the magnetoconductance through a clean interface is partly due to the fact that all nonchiral Landau levels perfectly reflect at the interface [13]. This is no longer strictly true if the momentum parallel to the interface is not conserved, as happens in the presence of disorder. We will now show that these corrections are negligible.

While we neglect the contributions of nonchiral Landau levels in the Landauer-Boltzmann approach, such contributions can in principle show up in the numerical transport simulations. In Fig. 4 we indeed observe a weak enhancement at small fields and intermediate ξ. In Fig. 5 the enhancement is also visible as a tiny zero-field conductance that increases with an increasing disorder strength.

The weakness of these corrections can be explained as follows. The number of (nonchiral) bulk modes that arrive at the interface area A is at most on the order of $\sim k_F^2 A$, where $k_F \ll L_{\rm arc}$ is the Fermi momentum measured from the Weyl node. This number decreases with increasing B due to an increased occupation of the zeroth Landau level. Since the overlap of bulk states of the right and left WSMs is much smaller than that of bulk and Fermi arcs, the rate of transmission of nonchiral bulk states is on the order of the scattering rate between the bulk and the Fermi arcs. The disorder-activated conductance can thus be estimated as $(e^2/h)k_F A^2/l_{\rm mfp}L_{\rm arc}$. Comparing with the anomalous magnetoconductance $G(B) \sim G_0(B)$ in Eq. (1), we find that the disorder-induced contribution of nonchiral levels becomes significant only if

$$\frac{1}{l_B^2} \lesssim \frac{k_F^2}{l_{\rm mfp}L_{\rm arc}}. \tag{25}$$

This explains why there is no significant effect in the case of weak disorder and well-separated Weyl nodes.

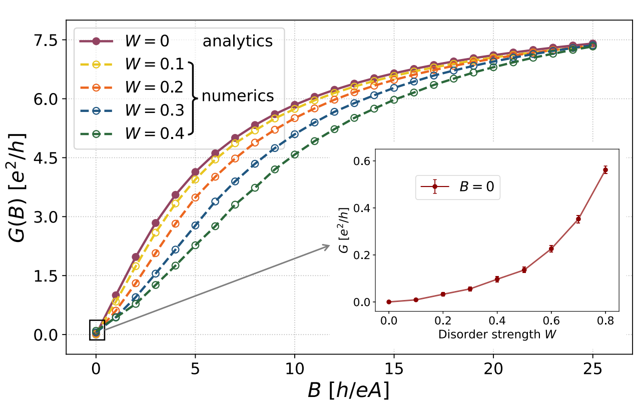

FIG. 5. Conductance of weakly coupled interfaces (exhibiting magnetic breakdown) for different (uncorrelated) disorder strength W at energy $E = 0.1$ and interface hopping strength $t = 0.1$. Disorder shows a weak suppression of the conductance, similar to the normal-interface case. Weak disorder-activated conductance of nonchiral Landau levels is visible as a small zero-field conductance, shown in the inset [37].

IV. DISCUSSION AND CONCLUSIONS

We have explored the robustness of the tunnel magnetoconductance across a WSM interface, which in the ideal limit of a clean interface is given by $G_0(B) = (e^3/h^2)|\boldsymbol{A}\cdot\boldsymbol{B}|$ for each homochiral (i.e., chirality-preserving) Fermi arc, where $|\boldsymbol{A}\cdot\boldsymbol{B}|$ is the magnetic flux through the interface of area $\boldsymbol{A}$. Our results show that disorder introduces two field regimes, above and below a characteristic field strength $B \approx B_{\mathrm{arc}}$, at which the Fermi-arc lifetime τ_{arc}—the mean time between inter-arc scattering events—is equal to the dwell time τ_{dwell}—the time a particle spends on the Fermi arc in the presence of a magnetic field. When the inter-arc scattering is dominated by spatially smooth disorder, B_{arc} goes to zero as $\sim e^{-\Delta^2\xi^2}$ with an increasing disorder correlation length ξ and an increasing separation of the Fermi arcs $\sim\Delta$.

In the low-field regime, $\tau_{\mathrm{arc}} \ll \tau_{\mathrm{dwell}}$, for a system with N_{L} (N_{R}) Weyl node pairs in the left (right) WSM, the low-field magnetoconductance will assume a simple fraction of the elementary conductance,

$$G(B) = \frac{N_{\mathrm{L}}N_{\mathrm{R}}}{N_{\mathrm{L}} + N_{\mathrm{R}}} G_0(B), \tag{26}$$

independent on the Fermi-arc connectivity. This result resembles the fractionally quantized conductance across a graphene *p-n* junction in the quantum Hall regime, where the role of motion along Fermi arcs in *momentum* space is played by motion along copropagating edge states along the junction in real space [35,36].

In the high-field regime ($\tau_{\mathrm{arc}} \gg \tau_{\mathrm{dwell}}$), we recover the clean-interface magnetoconductance. Here the crucial numbers are not the numbers of Weyl nodes but instead the number of *homochiral* Fermi-arc pairs N_{ho}—Fermi arcs that connect projections of Weyl nodes of the same chirality, which are then necessarily Weyl nodes from opposite sides of the interface. The magnetoconductance is then equal to

$$G(B) = N_{\mathrm{ho}} G_0(B). \tag{27}$$

The three integer parameters N_{ho}, N_{L}, and N_{R} can be independently controlled by the choice of the two interfaced WSM materials and the interface design. In this way, various differently shaped magnetoconductance behaviors can be experimentally realized.

To test and exemplify these predictions, we considered a minimal model of a single pair of Weyl nodes, which position shifts across the interface and the four node projections are connected by two homochiral Fermi arcs. The resulting magnetoconductance behavior, in particular showing a low- and high-field conductance of $G(B) = G_0(B)/2$ and $G(B) = G_0(B)$, respectively, was confirmed by comparing with numerical simulations on a lattice model.

In the experimental measurement of the longitudinal magnetoresistance in a grained WSM [12] with randomly oriented crystallites, a robust negative linear magnetoresistance has been observed across a large field range. The slope at fields below $\sim$1 T is approximately a factor of 2 smaller than the slope at larger fields. At fields far below the saturation field (no saturation is observed in the experiment), the corresponding magnetoconductance is minus the magnetoresistance, which thus qualitatively agrees with our theory. Since the number of Weyl nodes does not change across the grains, the slope difference by a factor 2 indicates, according to our analysis, that the interface Fermi arcs are predominantly homochiral. Note, however, that while the conductance is expected to be the same for all interfaces at low fields, it can differ at large fields since the number of homochiral Fermi arcs can vary.

Methodologically, we derived a semiclassical Landauer-Boltzmann theory, whose validity we confirmed by comparing with numerical transport simulations of a disordered system with both correlated and uncorrelated disorder at zero temperature. We expect the semiclassical theory to remain valid at finite temperatures, as well as for other perturbations, such as elastic and inelastic scattering off phonons. Our hybrid Landauer-Boltzmann theory can be easily extended to various scenarios to gain analytical insight or more efficient numerics (as compared to full-quantum calculations).

Qualitatively, we can infer that the temperature dependence of the anomalous magnetoconductance contribution is weak, since the energy dependence (in the range of separated Weyl fermions) is vanishing/weak. The energy dependence vanishes in the universal low- and high-field limits as the clean-system conductance $G_0(B)$ is energy independent [13]. In the crossover regime, the conductance could in general depend on energy through the energy dependence of the scattering and the dwell time but the conductance can only be modified by a strongly bounded factor $\in [0.5, 1]$.

ACKNOWLEDGMENTS

We thank Piet W. Brouwer and Zhiyang Tan for useful discussions. This work was supported by the Deutsche Forschungsgemeinschaft (DFG, German Research Foundation), Project No. 277101999; CRC-TR 183 (Project No. A02); and the Emmy Noether program, Project No. 506208038.

DATA AVAILABILITY

The data that support the findings of this article are openly available [37], embargo periods may apply.

APPENDIX: TRANSFER MATRICES

In this Appendix, we use transfer matrices to derive various quantities of interest for the model calculations based on the Landauer-Boltzmann approach, namely, the group velocity of the interface Fermi arcs and their wave-function overlap. Explicitly, we consider the Bloch Hamiltonians of the form

$$\mathcal{H}_A = \sin k_x \tau^x + \eta_y^A(\boldsymbol{k})\tau^y + [\mu(\boldsymbol{k}) - \cos k_x]\tau^z, \tag{A1}$$

where $\mu(\boldsymbol{k}) = (1 + 2\cos k_0 - \cos k_y - \cos k_z)$ and $A \in \{\mathrm{L}, \mathrm{R}\}$. To construct the corresponding generalized transfer matrix along x, we first rewrite the Hamiltonian as

$$\mathcal{H}_A(\boldsymbol{k}_{3d}) = J\,\mathrm{e}^{-\mathrm{i}k_x} + M_A(\boldsymbol{k}) + J^\dagger \mathrm{e}^{\mathrm{i}k_x}, \tag{A2}$$

where we identify the hopping and on-site matrices

$$J = \tfrac{1}{2}(\mathrm{i}\tau^x - \tau^z), \quad M_A = \eta_y^A(\boldsymbol{k})\tau^y + \mu(\boldsymbol{k})\tau^z.$$

The real-space Schrödinger equation takes the form of a recursion relation

$$(\varepsilon - M_A)\psi_n = J\psi_{n+1} + J^\dagger\psi_{n-1}. \tag{A3}$$

As J is singular, we follow the approach of [40], whereby we rewrite the recursion relation as

$$\psi_n = \mathcal{G}_A J\psi_{n+1} + \mathcal{G}_A J^\dagger\psi_{n-1}, \tag{A4}$$

where $\mathcal{G}_A = (\varepsilon - M_A)^{-1}$. Next, we compute the reduced singular value decomposition $J = \boldsymbol{v}\cdot\boldsymbol{w}^\dagger$, whereby $\boldsymbol{v}$ and $\boldsymbol{w}$ form an orthonormal basis of $\mathbb{C}^2$. Expanding the wave function as $\psi_n = \alpha_n\boldsymbol{v} + \beta_n\boldsymbol{w}$ with $\alpha_n, \beta_n \in \mathbb{C}$ and taking inner products of Eq. (A4) with $\boldsymbol{v}$ and $\boldsymbol{w}$, we get a pair of recursion relations for α_n and β_n, which can be cast in the transfer matrix form

$$\Phi_{n+1} = \mathcal{T}_A(\varepsilon, \boldsymbol{k})\Phi_n, \quad \Phi_n = \begin{pmatrix}\beta_n \\ \alpha_{n-1}\end{pmatrix}, \tag{A5}$$

with

$$\mathcal{T}_A(\varepsilon, \boldsymbol{k}) = \frac{1}{\mu}\begin{pmatrix}\varepsilon^2 - \left(\eta_y^A\right)^2 - \mu^2 & -\varepsilon + \eta_y^A \\ \varepsilon + \eta_y^A & -1\end{pmatrix}. \tag{A6}$$

To derive the interface modes, we briefly recap the approach of Ref. [15]. Assuming the interface lies at $n = 0$ and the coupling across the interface is scaled by $t \in [0, 1]$, the recursion relation of Eq. (A3) for $n = 0, 1$ becomes

$$\begin{aligned}(\varepsilon - M_\mathrm{L})\psi_0 &= tJ\psi_1 + J^\dagger\psi_{-1},\\ (\varepsilon - M_\mathrm{R})\psi_1 &= J\psi_2 + tJ^\dagger\psi_0.\end{aligned} \tag{A7}$$

Again expanding ψ_n in the $(\boldsymbol{v}, \boldsymbol{w})$ basis, we can combine these equations into

$$\begin{aligned}\Phi_1 &= \mathrm{diag}\{t^{-1}, 1\}\mathcal{T}_\mathrm{L}\Phi_0,\\ \Phi_2 &= \mathcal{T}_\mathrm{R}\mathrm{diag}\{1, t\}\Phi_2,\end{aligned} \tag{A8}$$

so that

$$\Phi_2 = \mathcal{T}_\mathrm{R}\mathcal{K}\mathcal{T}_\mathrm{L}\Phi_0, \quad \mathcal{K} = \mathrm{diag}\{t^{-1}, t\}. \tag{A9}$$

For a state to be localized at the interface, it must decay exponentially on either side of the interface, so that Φ_0 and Φ_2 must be eigenvectors of $\mathcal{T}_{\mathrm{L/R}}$ with eigenvalues $\rho_{\mathrm{L/R}}$, respectively. Using the relation between Φ_0 and Φ_2, we can rewrite

$$\begin{aligned}\rho_\mathrm{R}\Phi_0 &= (\mathcal{T}_\mathrm{R}\mathcal{K}\mathcal{T}_\mathrm{L})^{-1}\mathcal{T}_\mathrm{R}(\mathcal{T}_\mathrm{R}\mathcal{K}\mathcal{T}_\mathrm{L})\Phi_0\\ &= \left(\mathcal{T}_\mathrm{L}^{-1}\mathcal{K}^{-1}\mathcal{T}_\mathrm{R}\mathcal{K}\mathcal{T}_\mathrm{L}\right)\Phi_0,\end{aligned} \tag{A10}$$

so that Φ_0 is a simultaneous eigenvector of the matrices $\mathcal{T}_\mathrm{L}$ and $\mathcal{T}_\mathrm{L}^{-1}\mathcal{K}^{-1}\mathcal{T}_\mathrm{R}\mathcal{K}\mathcal{T}_\mathrm{L}$. A necessary condition for such a simultaneous eigenvector to exist is given by [15]

$$F(\varepsilon, \boldsymbol{k}) \equiv \det[\mathcal{T}_\mathrm{L}, \mathcal{K}^{-1}\mathcal{T}_\mathrm{R}\mathcal{K}] = 0. \tag{A11}$$

To derive the interface states, we need to solve this implicit relation between ε and $\boldsymbol{k}$. We now describe the computation of various quantities of interest for the semiclassics.

1. Group velocity of the interface Fermi arcs

To compute the group velocity of the interface Fermi arcs from the transfer matrices, we note that there exists an interface mode at momentum $\boldsymbol{k}$ and energy ε if $F(\varepsilon, \boldsymbol{k}) = 0$ [see Eq. (A11)]. If $\varepsilon + \delta\varepsilon$ and $\boldsymbol{k} + \delta\boldsymbol{k}$ also satisfy this condition, then at linear order, we get

$$\left[\delta\varepsilon\frac{\partial}{\partial\varepsilon} + \delta\boldsymbol{k}\cdot\nabla_{\boldsymbol{k}}\right]F(\varepsilon, \boldsymbol{k}) = 0. \tag{A12}$$

Thus, the group velocity is given by

$$\boldsymbol{v} = \nabla_{\boldsymbol{k}}\varepsilon = -\frac{\nabla_{\boldsymbol{k}}F(\varepsilon, \boldsymbol{k})}{\partial_\varepsilon F(\varepsilon, \boldsymbol{k})}. \tag{A13}$$

Having computed the Fermi arc for a given chemical potential, we can numerically evaluate this expression to obtain the velocity for each point on the Fermi arc.

2. Wave-function overlap

The transition probability for a disorder-induced scattering $\boldsymbol{k} \to \boldsymbol{k}'$ depends on the overlap within the interface layers of the interface modes with transverse momenta $\boldsymbol{k}_{1,2}$. Explicitly, given the *unnormalized* wave functions $|\Psi\rangle$ and $|\Psi'\rangle$ with $|\Psi\rangle \equiv \sum_n \psi_n |n\rangle$, etc., we need to compute

$$\langle\Psi|\Psi'\rangle_\mathrm{int} = \frac{\psi_0^\dagger\psi_0' + \psi_1^\dagger\psi_1'}{\sqrt{\langle\Psi|\Psi\rangle\,\langle\Psi'|\Psi'\rangle}}, \tag{A14}$$

where the sum is only over the interface layers $n = 0, 1$.

We now describe the explicit computation of these states from the eigenvalues and eigenvectors of the transfer matrix. Note that an interface state with energy ε exists for a given $\boldsymbol{k}$ only if Eq. (A11) holds, i.e., only if $\ker[\mathcal{T}_\mathrm{L}, K^{-1}\mathcal{T}_\mathrm{R}K]$ is nontrivial. Let $[\mathcal{T}_\mathrm{L}, \mathcal{K}^{-1}\mathcal{T}_\mathrm{R}\mathcal{K}]\varphi = 0$ for a $\varphi \in \mathbb{C}^2$, so that φ satisfies

$$\mathcal{T}_\mathrm{L}\varphi = \rho_\mathrm{L}\varphi, \quad \mathcal{K}^{-1}\mathcal{T}_\mathrm{R}\mathcal{K}\varphi = \rho_\mathrm{R}\varphi. \tag{A15}$$

These can be used to compute

$$\Phi_n = \begin{cases}\rho_\mathrm{L}^n\varphi, & n \leqslant 0,\\ \rho_\mathrm{L}\,\mathrm{diag}\{t^{-1}, 1\}\varphi, & n = 1,\\ \rho_\mathrm{L}\rho_\mathrm{R}^{n-1}\mathcal{K}\varphi, & n \geqslant 2.\end{cases} \tag{A16}$$

Similarly, let φ' be the corresponding vector for $\boldsymbol{k}'$, from which we can compute Φ_n'. We next seek to rewrite Eq. (A14) in terms of Φ_n. We first compute the numerator as

$$\begin{aligned}\sum_{n=0}^{1}\psi_n^*\psi_n' &= \sum_{n=0}^{1}(\alpha_n^*\boldsymbol{v}^\dagger + \beta_n^*\boldsymbol{w}^\dagger)(\alpha_n'\boldsymbol{v} + \beta_n'\boldsymbol{w})\\ &= \sum_{n=0}^{1}\alpha_n^*\alpha_n' + \beta_n^*\beta_n',\end{aligned} \tag{A17}$$

where we have used the orthonormality of $\boldsymbol{v}$ and $\boldsymbol{w}$. Setting $\varphi = (\varphi_1, \varphi_2)^T$, we identify $\alpha_0 = \rho_\mathrm{L}\varphi_2$, $\beta_0 = \varphi_1$, $\alpha_1 = \rho_\mathrm{L}\rho_\mathrm{R}t\varphi_2$, and $\beta_1 = \rho_\mathrm{L}t^{-1}\varphi_1$ and similarly for φ'. Thus,

$$\sum_{n=0}^{1}\psi_n^*\psi_n' = (1 + t^{-2}\rho_\mathrm{L}^*\rho_\mathrm{L}')\varphi_1^*\varphi_1' + \rho_\mathrm{L}^*\rho_\mathrm{L}'(1 + t^2\rho_\mathrm{R}^*\rho_\mathrm{R}')\varphi_2^*\varphi_2'. \tag{A18}$$

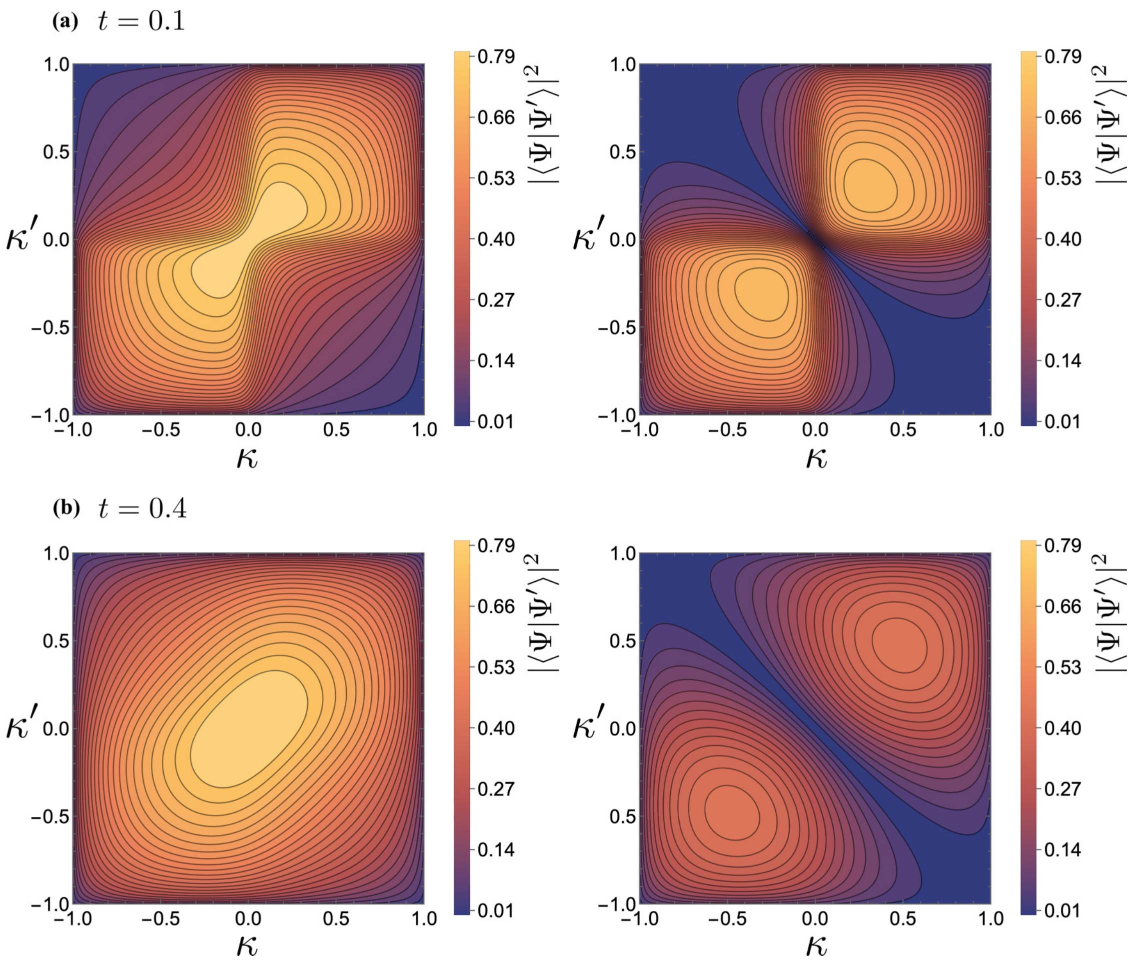

FIG. 6. Overlap of Fermi-arc wave functions $|\langle\Psi|\Psi'\rangle|^2$ for intra-arc (left) and inter-arc (right) scattering for $\varepsilon = 0$ and tunneling parameter (a) $t = 0.1$ and (b) $t = 0.4$.

Similarly, we compute the normalization constant as

$$\langle\Psi|\Psi\rangle = \sum_{n=-\infty}^{\infty} |\Psi_n|^2 = \sum_{n=-\infty}^{\infty} (|\alpha_n|^2 + |\beta_n|^2) = \sum_{n=-\infty}^{\infty} |\Phi_n|^2 \equiv \varphi^\dagger \mathcal{O} \varphi, \tag{A19}$$

where we have set

$$\begin{aligned} \mathcal{O} &= \sum_{n=-\infty}^{0} |\rho_{\rm L}|^{2n} + |\rho_{\rm L}|^2 \mathrm{diag}\{t^{-1}, 1\}^2 + |\rho_{\rm L}|^2 \mathcal{K}^2 \sum_{n=2}^{\infty} |\rho_{\rm R}|^{2(n-1)} \\ &= |\rho_{\rm L}|^2 \mathrm{diag}\left\{ \frac{1}{|\rho_{\rm L}|^2 - 1} + \frac{t^{-2}}{1 - |\rho_{\rm R}|^2}, \; \frac{|\rho_{\rm L}|^2}{|\rho_{\rm L}|^2 - 1} + \frac{t^2 |\rho_{\rm R}|^2}{1 - |\rho_{\rm R}|^2} \right\}. \end{aligned} \tag{A20}$$

Note that this matrix is positive definite, since for a localized mode, we must have $|\rho_{\rm L}| > 1$ and $|\rho_{\rm R}| < 1$. Substituting Eqs. (A18) and (A19) in (A14) then yields the desired overlaps. The result is shown in Fig. 6.

[1] X. Wan, A. M. Turner, A. Vishwanath, and S. Y. Savrasov, Topological semimetal and Fermi-arc surface states in the electronic structure of pyrochlore iridates, Phys. Rev. B **83**, 205101 (2011).
[2] N. P. Armitage, E. J. Mele, and A. Vishwanath, Weyl and Dirac semimetals in three-dimensional solids, Rev. Mod. Phys. **90**, 015001 (2018).
[3] S. L. Adler, Axial-vector vertex in spinor electrodynamics, Phys. Rev. **177**, 2426 (1969).
[4] J. S. Bell and R. Jackiw, A PCAC Puzzle: $\pi^0 \to \gamma\gamma$ in the σ-model, Nuovo Cimento A **60**, 47 (1969).
[5] D. T. Son and B. Z. Spivak, Chiral anomaly and classical negative magnetoresistance of Weyl metals, Phys. Rev. B **88**, 104412 (2013).

[6] A. A. Burkov, Weyl metals, Annu. Rev. Condens. Matter Phys. **9**, 359 (2018).

[7] J. Xiong, S. K. Kushwaha, T. Liang, J. W. Krizan, M. Hirschberger, W. Wang, R. J. Cava, and N. P. Ong, Evidence for the chiral anomaly in the Dirac semimetal Na_3 Bi, Science **350**, 413 (2015).

[8] A. Altland and D. Bagrets, Theory of the strongly disordered Weyl semimetal, Phys. Rev. B **93**, 075113 (2016).

[9] R. D. dos Reis, M. O. Ajeesh, N. Kumar, F. Arnold, C. Shekhar, M. Naumann, M. Schmidt, M. Nicklas, and E. Hassinger, On the search for the chiral anomaly in Weyl semimetals: The negative longitudinal magnetoresistance, New J. Phys. **18**, 085006 (2016).

[10] M. Naumann, F. Arnold, M. D. Bachmann, K. A. Modic, P. J. W. Moll, V. Süß, M. Schmidt, and E. Hassinger, Orbital effect and weak localization in the longitudinal magnetoresistance of Weyl semimetals NbP, NbAs, TaP, and TaAs, Phys. Rev. Mater. **4**, 034201 (2020).

[11] B. Q. Lv, T. Qian, and H. Ding, Experimental perspective on three-dimensional topological semimetals, Rev. Mod. Phys. **93**, 025002 (2021).

[12] D. Zhang, W. Jiang, H. Yun, O. J. Benally, T. Peterson, Z. Cresswell, Y. Fan, Y. Lv, G. Yu, J. G. Barriocanal, *et al.*, Robust negative longitudinal magnetoresistance and spin–orbit torque in sputtered Pt_3Sn and $Pt_3Sn_xFe_{1-x}$ topological semimetal, Nat. Commun. **14**, 4151 (2023).

[13] A. Y. Chaou, V. Dwivedi, and M. Breitkreiz, Magnetic breakdown and chiral magnetic effect at Weyl-semimetal tunnel junctions, Phys. Rev. B **107**, L241109 (2023).

[14] A. Y. Chaou, V. Dwivedi, and M. Breitkreiz, Quantum oscillation signatures of interface Fermi arcs, Phys. Rev. B **110**, 035116 (2024).

[15] V. Dwivedi, Fermi arc reconstruction at junctions between Weyl semimetals, Phys. Rev. B **97**, 064201 (2018).

[16] G. Murthy, H. A. Fertig, and E. Shimshoni, Surface states and arcless angles in twisted Weyl semimetals, Phys. Rev. Res. **2**, 013367 (2020).

[17] F. Abdulla, S. Rao, and G. Murthy, Fermi arc reconstruction at the interface of twisted Weyl semimetals, Phys. Rev. B **103**, 235308 (2021).

[18] S. Kaushik, I. Robredo, N. Mathur, L. M. Schoop, S. Jin, M. G. Vergniory, and J. Cano, Transport signatures of Fermi arcs at twin boundaries in Weyl materials, Phys. Rev. B **111**, 085133 (2025).

[19] F. Buccheri, R. Egger, and A. De Martino, Transport, refraction, and interface arcs in junctions of Weyl semimetals, Phys. Rev. B **106**, 045413 (2022).

[20] N. Mathur, F. Yuan, G. Cheng, S. Kaushik, I. Robredo, and G. Maia, Atomically sharp internal interface in a chiral Weyl semimetal nanowire, Nano Lett. **23**, 2695 (2023).

[21] R. Kundu, H. A. Fertig, and A. Kundu, Broken symmetry and competing orders in Weyl semimetal interfaces, Phys. Rev. B **107**, L041402 (2023).

[22] M. Breitkreiz and P. W. Brouwer, Fermi-arc metals, Phys. Rev. Lett. **130**, 196602 (2023).

[23] M. Breitkreiz and P. W. Brouwer, Large contribution of Fermi arcs to the conductivity of topological metals, Phys. Rev. Lett. **123**, 066804 (2019).

[24] C. Zhang, Z. Ni, J. Zhang, X. Yuan, Y. Liu, Y. Zou, Z. Liao, Y. Du, A. Narayan, H. Zhang, T. Gu, X. Zhu, L. Pi, S. Sanvito, X. Han, J. Zou, Y. Shi, X. Wan, S. Y. Savrasov, and F. Xiu, Ultrahigh conductivity in Weyl semimetal NbAs nanobelts, Nat. Mater. **18**, 482 (2019).

[25] P. M. Perez-Piskunow, N. Bovenzi, A. R. Akhmerov, and M. Breitkreiz, Chiral anomaly trapped in Weyl metals: Nonequilibrium valley polarization at zero magnetic field, SciPost Phys. **11**, 046 (2021).

[26] N. A. Lanzillo, U. Bajpai, and C.-T. Chen, Topological semimetal interface resistivity scaling for vertical interconnect applications, Appl. Phys. Lett. **124**, 181603 (2024).

[27] I. A. Leahy, A. D. Rice, C.-S. Jiang, G. Paul, K. Alberi, and J. N. Nelson, Anisotropic weak antilocalization in thin films of the Weyl semimetal TaAs, Phys. Rev. B **110**, 054206 (2024).

[28] A. I. Khan, A. Ramdas, E. Lindgren, H.-M. Kim, B. Won, X. Wu, K. Saraswat, C.-T. Chen, Y. Suzuki, F. H. da Jornada, I.-K. Oh, and E. Pop, Surface conduction and reduced electrical resistivity in ultrathin noncrystalline NbP semimetal, Science **387**, 62 (2025).

[29] S. Kumar, Y.-H. Tu, S. Luo, N. A. Lanzillo, T.-R. Chang, G. Liang, R. Sundararaman, H. Lin, and C.-T. Chen, Surface-dominated conductance scaling in Weyl semimetal NbAs, npj Comput. Mater. **10**, 84 (2024).

[30] V. Kaladzhyan and J. H. Bardarson, Quantized Fermi arc mediated transport in Weyl semimetal nanowires, Phys. Rev. B **100**, 085424 (2019).

[31] G. Resta, S.-T. Pi, X. Wan, and S. Y. Savrasov, High surface conductivity of Fermi-arc electrons in Weyl semimetals, Phys. Rev. B **97**, 085142 (2018).

[32] E. V. Gorbar, V. A. Miransky, I. A. Shovkovy, and P. O. Sukhachov, Origin of dissipative Fermi arc transport in Weyl semimetals, Phys. Rev. B **93**, 235127 (2016).

[33] J. H. Wilson, J. H. Pixley, D. A. Huse, G. Refael, and S. Das Sarma, Do the surface Fermi arcs in Weyl semimetals survive disorder?, Phys. Rev. B **97**, 235108 (2018).

[34] W. Kohn and J. Luttinger, Quantum theory of electrical transport phenomena, Phys. Rev. **108**, 590 (1957).

[35] J. R. Williams, L. DiCarlo, and C. M. Marcus, Quantum Hall effect in a gate-controlled *p-n* junction of graphene, Science **317**, 638 (2007).

[36] D. A. Abanin and L. S. Levitov, Quantized transport in graphene *p-n* junctions in a magnetic field, Science **317**, 641 (2007).

[37] H. Tian, A. Y. Chaou, V. Dwivedi, and M. Breitkreiz, Code and data associated with the paper "magnetotransport across Weyl semimetal grain boundaries," Zenodo (2026), doi: 10.5281/zenodo.17961585.

[38] C. W. Groth, M. Wimmer, A. R. Akhmerov, and X. Waintal, Kwant: A software package for quantum transport, New J. Phys. **16**, 063065 (2014).

[39] A. Potter, I. Kimchi, and A. Vishwanath, Quantum oscillations from surface Fermi-arcs in Weyl and Dirac semi-metals, Nat. Commun. **5**, 5161 (2014).

[40] V. Dwivedi and V. Chua, Of bulk and boundaries: Generalized transfer matrices for tight-binding models, Phys. Rev. B **93**, 134304 (2016).